

Copyright WILEY-VCH Verlag GmbH & Co. KGaA, 69469 Weinheim, Germany, 2020.



Supporting Information

for *Adv. Mater. Interfaces*, DOI: 10.1002/admi.202000425

Lithium Garnet $\text{Li}_7\text{La}_3\text{Zr}_2\text{O}_{12}$ Electrolyte for All-Solid-State Batteries: Closing the Gap between Bulk and Thin Film Li-Ion Conductivities

Jordi Sastre, Agnieszka Priebe, Max Döbeli, Johann Michler, Ayodhya N. Tiwari, and Yaroslav E. Romanyuk*

Supporting Information:

Lithium garnet $\text{Li}_7\text{La}_3\text{Zr}_2\text{O}_{12}$ electrolyte for all-solid-state batteries: closing the gap between bulk and thin film Li-ion conductivities

Jordi Sastre,^{*,†} Agnieszka Priebe,[‡] Max Döbeli,[¶] Johann Michler,[‡] Ayodhya N. Tiwari,[†] and Yaroslav E. Romanyuk[†]

[†]*Laboratory for Thin Films and Photovoltaics, Empa - Swiss Federal Laboratories for Materials Science and Technology, Überlandstrasse 129, CH-8600 Dübendorf, Switzerland*

[‡]*Laboratory for Mechanics of Materials and Nanostructures, Empa - Swiss Federal Laboratories for Materials Science and Technology, Feuerwerkerstrasse 39, CH-3602 Thun, Switzerland*

[¶]*Ion Beam Physics, ETH Zürich - Swiss Federal Institute of Technology, Otto-Stern-Weg 5, CH-8093 Zürich, Switzerland*

E-mail: jordi.sastrepellicer@empa.ch

Phone: +41 58 765 61 10

Table S1: Stoichiometry determined by ICP-MS of the doped LLZO targets employed in the sputtering deposition process.

	Li	La	Zr	Al	Ga
Al-LLZO	6.32	2.94	2.01	0.23	-
Ga-LLZO	6.28	2.94	2.01	-	0.27

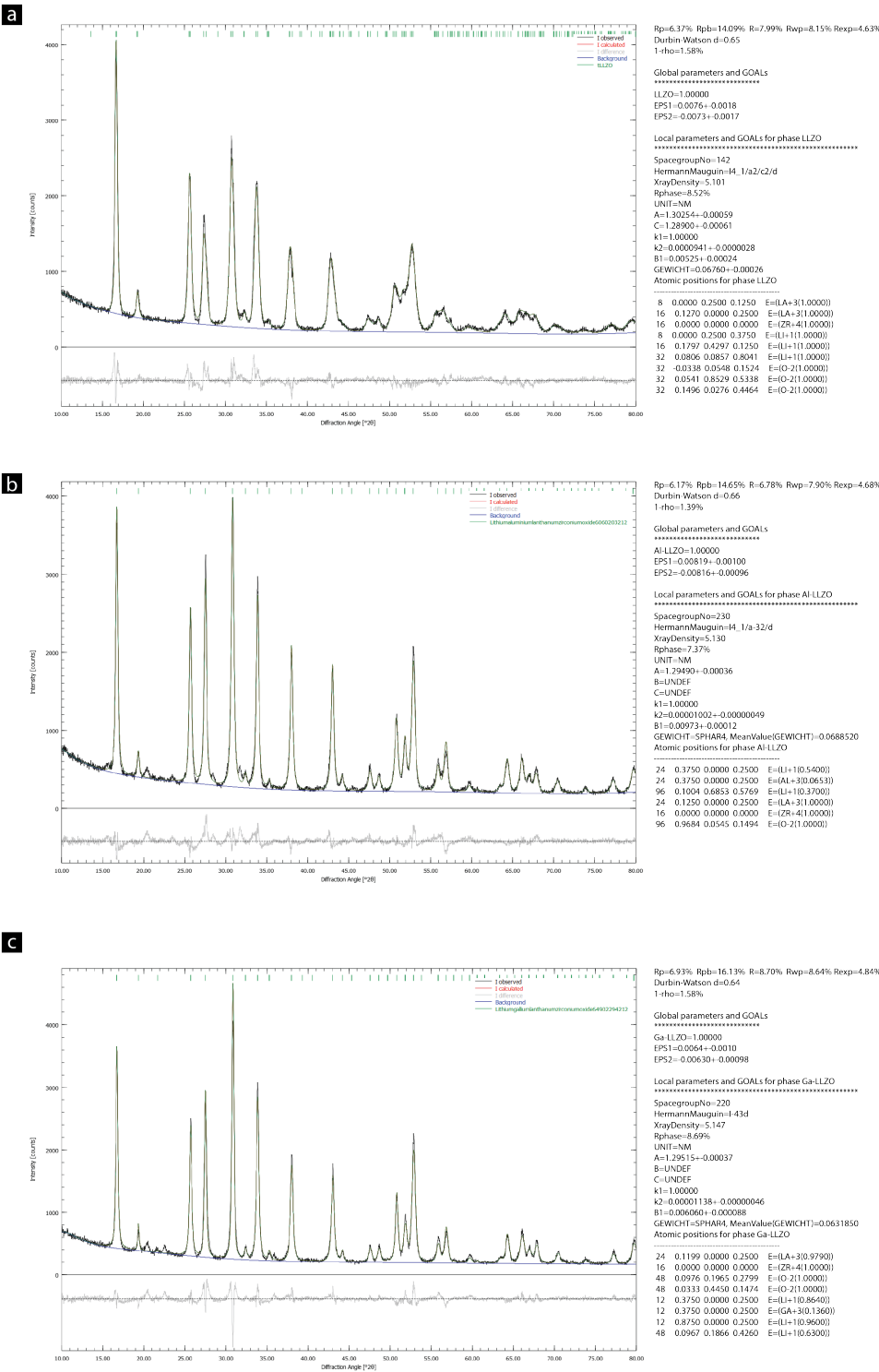


Figure S1: Rietveld refinements of the GI-XRD patterns obtained from the (a) non-doped, (b) Al-doped and (c) Ga-doped LLZO films.

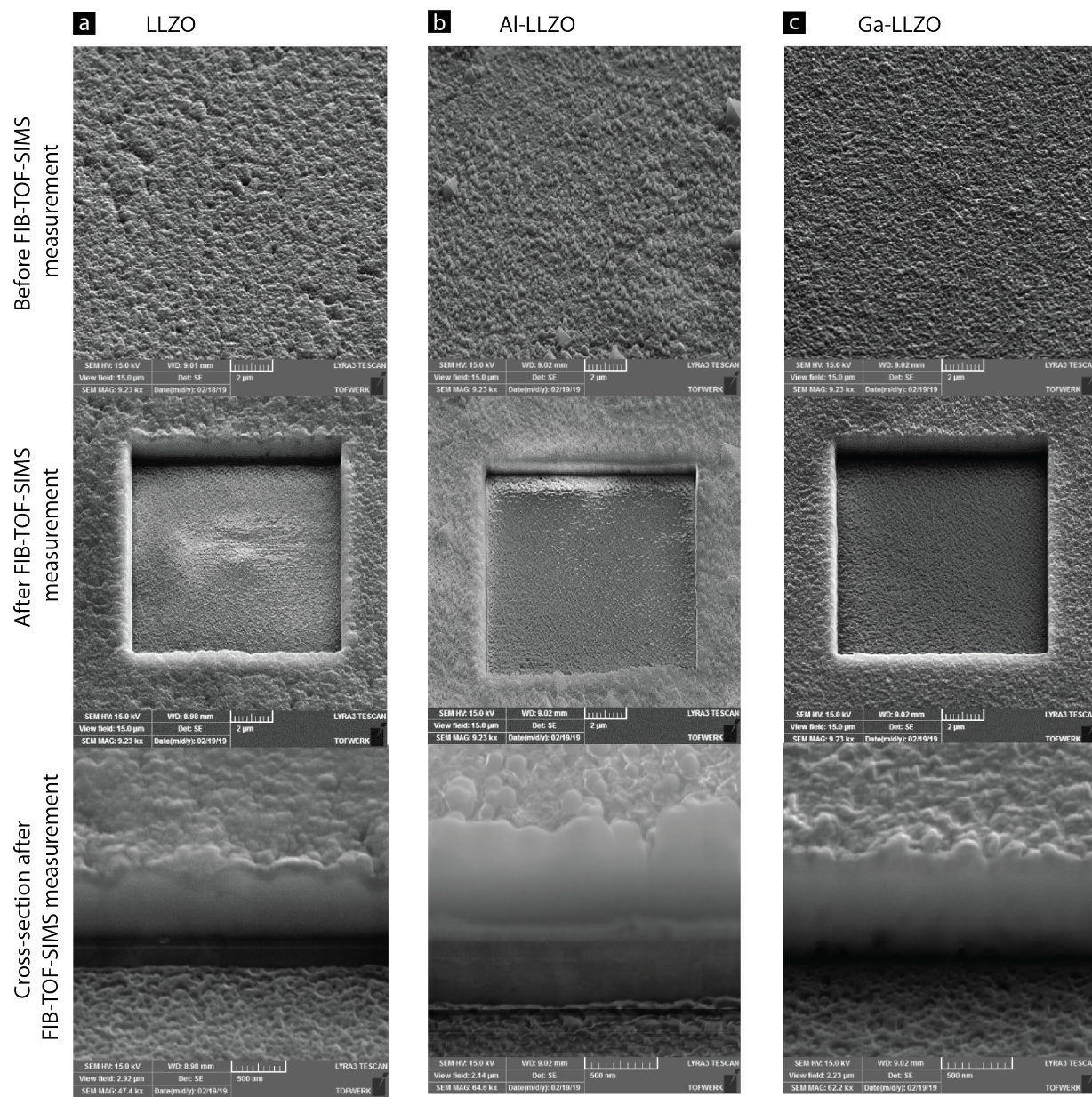


Figure S2: SEM images of the film's surface before and after the FIB-TOF-SIMS measurement, from the (a) non-doped, (b) Al-doped and (c) Ga-doped LLZO films.

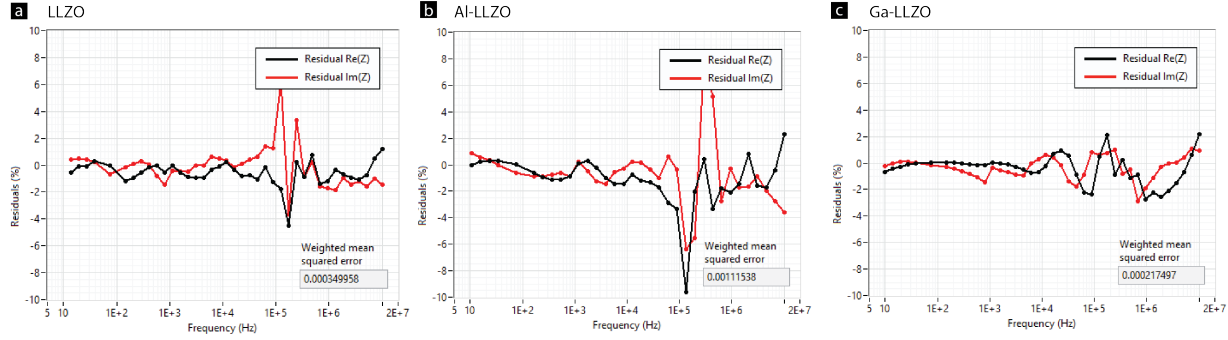


Figure S3: Residuals of the equivalent circuit fitting of the complex impedance spectra measured at room temperature in the the (a) non-doped, (b) Al-doped and (c) Ga-doped LLZO films.

Complex electric modulus

Following the Almond and West formalism,^{S1,S2} the complex electric modulus $M^*(\omega)$ can be useful to extract the dc conductivity in ionic conductors avoiding surface effects that typically dominate at low frequencies in the Nyquist plot of the complex impedance.

Experimentally, $M^*(\omega)$ can be derived from the complex impedance $Z^*(\omega)$ as:

$$M^*(\omega) = i\omega C_0 Z^*(\omega) = \frac{i\omega \varepsilon_0 Z^*(\omega)}{k}$$

where ω is the angular frequency, $C_0 = \varepsilon_0/k$ is the vacuum capacitance, ε_0 is the free-space permittivity and k is the geometric factor ($k = \frac{l}{w \cdot t}$).

$M^*(\omega)$ is related to the complex permittivity ε^* as:

$$M^*(\omega) = \frac{1}{\varepsilon^*(\omega)} = \frac{i\omega \varepsilon_0}{\sigma^*(\omega)}$$

Assuming that the ion dynamics are independent of frequency, ε^* can be defined as:

$$\varepsilon^*(\omega) = \varepsilon_\infty - \frac{i\sigma_{dc}}{\omega \varepsilon_0}$$

where ε_∞ is the high-frequency dielectric constant and σ_{dc} , the dc conductivity.

Combining both equations:

$$M^*(\omega) = \frac{1}{\varepsilon_\infty - \frac{i\sigma_{dc}}{\omega\varepsilon_0}}$$

Separating the real $M'(\omega)$ and imaginary $M''(\omega)$ parts, the complex modulus can be reformulated as:

$$M^*(\omega) = M'(\omega) + iM''(\omega) = \frac{\varepsilon_\infty}{\varepsilon_\infty^2 + (\frac{\sigma_{dc}}{\omega\varepsilon_0})^2} + i\frac{\frac{\sigma_{dc}}{\omega\varepsilon_0}}{\varepsilon_\infty^2 + (\frac{\sigma_{dc}}{\omega\varepsilon_0})^2}$$

At high frequencies, $M'(\omega) \xrightarrow[\omega \rightarrow \infty]{} \frac{1}{\varepsilon_\infty}$ and $M''(\omega) \xrightarrow[\omega \rightarrow \infty]{} 0$. Therefore, it is possible to obtain ε_∞ by extrapolating the intercept of the complex electric modulus with the real axis at high frequencies M'_{interc} (see upper plots in Figure S4, the red line is the fit used for the extrapolation and the orange dot is the intercept with the real axis).

From the plot of $M''(\omega)$ vs. ω (see lower plots in Figure S4), it is evident that $M''(\omega)$ peaks at a certain frequency ω_{max} . Looking at the equation of the imaginary part of $M^*(\omega)$:

$$M''(\omega) = \frac{\frac{\sigma_{dc}}{\omega\varepsilon_0}}{\varepsilon_\infty^2 + (\frac{\sigma_{dc}}{\omega\varepsilon_0})^2} = \frac{1}{\varepsilon_\infty} \frac{\frac{\sigma_{dc}}{\omega\varepsilon_0\varepsilon_0}}{1 + (\frac{\sigma_{dc}}{\omega\varepsilon_0\varepsilon_0})^2}$$

We can determine that this quantity will be maximum when $\frac{\sigma_{dc}}{\omega_{max}\varepsilon_0\varepsilon_0} = 1$.

From M'_{interc} and ω_{max} , the dc conductivity can be then calculated as:

$$\sigma_{dc} = \omega_{max}\varepsilon_0\varepsilon_0 = \frac{\omega_{max}\varepsilon_0}{M'_{interc}}$$

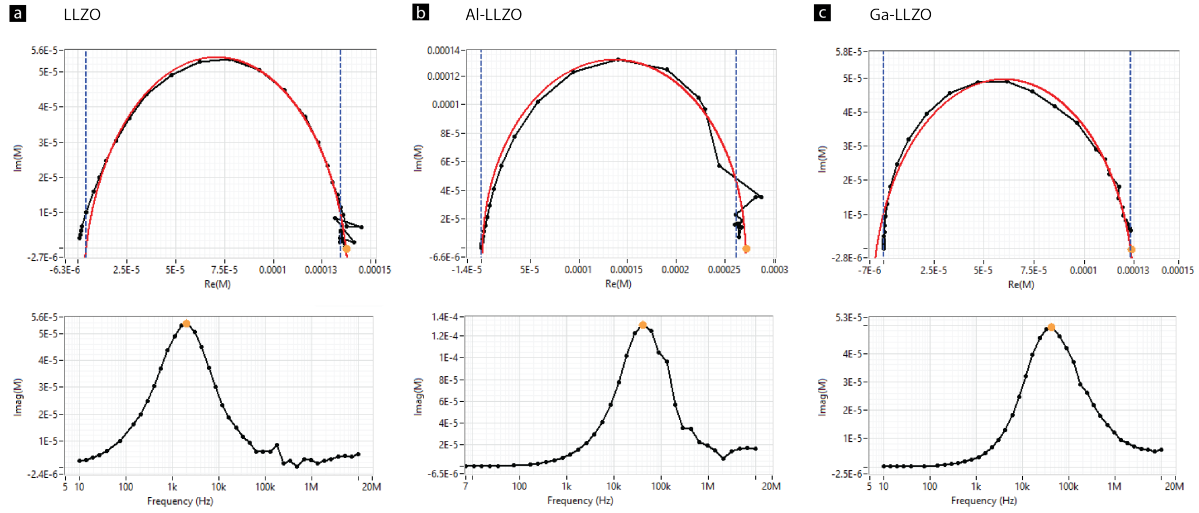


Figure S4: Fitting of the complex electric modulus measured at room temperature in the (a) non-doped, (b) Al-doped and (c) Ga-doped LLZO films.

Table S2: Effective ionic conductivities at room temperature extracted from the fitting of the electric modulus.

	$\sigma_{\text{eff}} \text{ (S/cm)}$
LLZO	6.42×10^{-6}
Al-LLZO	7.90×10^{-5}
Ga-LLZO	2.06×10^{-4}

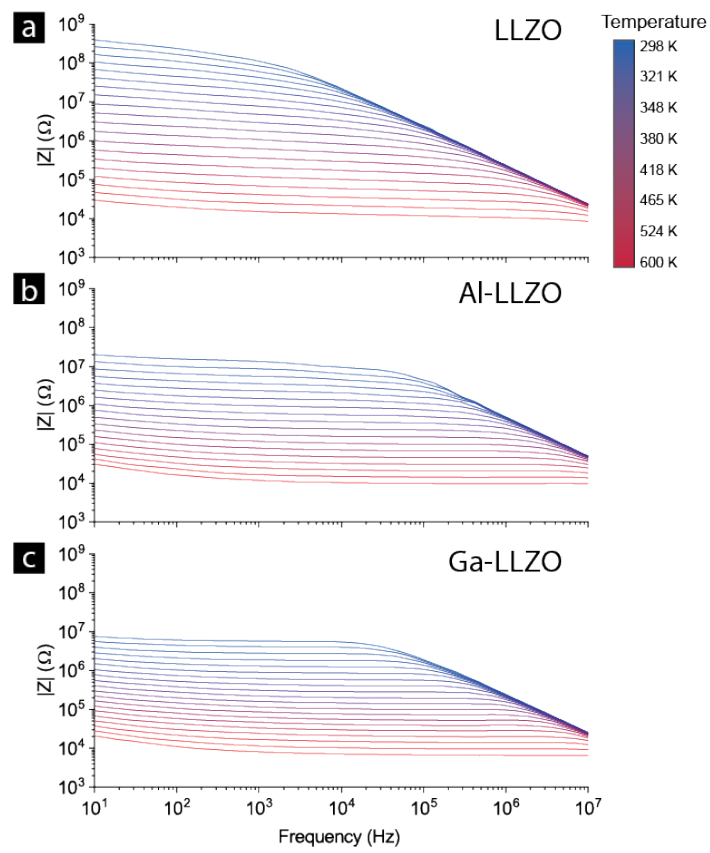


Figure S5: Modulus of the complex impedance measured at different temperatures in the the (a) non-doped, (b) Al-doped and (c) Ga-doped LLZO films.

Table S3: Literature review of LLZO samples: form, fabrication or deposition method, substitutional element, processing temperature, dwell time, phase after annealing, Li-ion conductivity at RT (temperature in parenthesis if different than 25°C), activation energy and thickness.

Ref.	Form	Fabrication / deposition method	Substitutional element	Processing temperature (°C)	Dwell (h)	Phase	Conductivity at RT (S cm ⁻¹)	Activation energy (eV)	Thickness (μm)
S3	Pellet	Nebulized spray pyrolysis	Al	1000	1	Cubic	4.40E-06	0.49	500
S4	Pellet	Solid-state reaction	Al	1180	35	Cubic	1.20E-04	0.37	700
S5	Pellet	Solid-state reaction	Al	1000	36	Cubic	1.40E-04 (30°C)	0.35	1000
S6	Pellet	Polymerized complex (Pechini)	Al	1200	6	Cubic	2.00E-04		3200
S7	Pellet	Solid-state reaction	Al	1300	1	Cubic	2.10E-04	0.33	
S8	Pellet	Solid-state reaction	Al	900	24	Cubic	2.11E-04	0.336	
S9	Pellet	Solid-state reaction	Al	1200	24	Cubic	2.25E-04	0.33	
S10	Pellet	Solid-state reaction	Al	1230	36	Cubic	2.40E-04		2200
S11	Pellet	Solid-state reaction + Hot pressing	Al	1160	2	Cubic	2.42E-04	0.37	800
S12	Pellet	Solid-state reaction	Al	1180	36	Cubic	2.99E-04		1000
S13	Pellet	Solid-state reaction	Al	1230	6	Cubic	3.00E-04	0.314	
S14	Pellet	Nebulized spray pyrolysis + FAST	Al	950	0.17	Cubic	3.30E-04	0.38	
S15	Pellet	Solid-state reaction + Hot pressing	Al	1050	4	Cubic	3.40E-04 (20°C)		
S16	Pellet	Solid-state reaction	Al	1200	40	Cubic	3.42E-04	0.25	1000
S17	Pellet	Sol-gel	Al	1175		Cubic	3.50E-04		1000
S18	Pellet	Solid-state reaction	Al	1230	30	Cubic	4.00E-04	0.34	
S19	Pellet	Solid-state reaction	Al	1000	5	Cubic	4.00E-04	0.26	2000
S20	Pellet	Solid-state reaction	Al	1070	10	Cubic	4.00E-04	0.28	1500
S21	Pellet	Solid-state reaction + FAST	Al	1150	0.05	Cubic	5.56E-04 (20°C)	0.29	1750
S22	Pellet	Solid-state reaction + FAST	Al	1150	0.05	Cubic	5.70E-04	0.3	1500
S23	Pellet	Sol-gel	Al (from crucible)	1200	36	Cubic	1.40E-04	0.34	2900
S24	Pellet	Solid-state reaction	Al (from crucible)	1230	35	Cubic	3.59E-04 (30°C)	0.41	
S25	Pellet	Solid-state reaction	Al (from crucible)	1230	36	Cubic	7.74E-04	0.3	1800
S26	Pellet	Solid-state reaction	Al, Pt	1200	24	Cubic	4.48E-04	0.32	
S10	Pellet	Solid-state reaction	Al, Si	1230	36	Cubic	6.80E-04		1600
S27	Pellet	Solid-state reaction	Ce	1000	4	Cubic	1.40E-05 (23°C)	0.48	
S28	Pellet	Solid-state reaction	Ga	1000	1	Cubic	3.50E-04		1000
S29	Pellet	Sol-gel	Ga	1085	6	Cubic	5.40E-04 (20°C)	0.35	5000
S17	Pellet	Sol-gel	Ga	1150		Cubic	7.50E-04		1000
S30	Pellet	Solid-state reaction	Ga	1000	12	Cubic	9.60E-04	0.32	1000
S31	Pellet	Solid-state reaction	Ga	1200	12	Cubic	1.00E-03		
S32	Pellet	Solid-state reaction	Ga	1085	6	Cubic	1.30E-03 (24°C)	0.3	
S13	Pellet	Solid-state reaction	Ga	1230	6	Cubic	1.32E-03	0.256	
S33	Pellet	Sol-gel	H ₂ O + CO ₂	450	20	LT-Cubic	3.10E-07	0.43	
S34	Pellet	1-step solution synthesis	H ₂ O + CO ₂	750	4	LT-Cubic	2.85E-06	0.36	1000
S35	Pellet	Solid-state reaction	Nb	1200	36	Cubic	8.00E-04	0.31	2000
S36	Pellet	Modified sol-gel Pechini	None	800	5	Tetragonal	3.12E-07	0.67	2000
S37	Pellet	Solid-state reaction	None	980	5	Tetragonal	1.63E-06	0.54	970
S38	Pellet	Citrate-nitrate	None	900	3	Tetragonal	5.19E-06 (20°C)	0.48	
S39	Pellet	Solid-state reaction + Hot pressing	None	1050	1	Tetragonal	2.30E-05	0.41	1000
S40	Pellet	Solid-state reaction	Sb	1100	24	Cubic	7.70E-04 (30°C)	0.34	
S41	Pellet	Solid-state reaction	Sr, Al (from crucible)	1200	24	Cubic	4.50E-04 (24°C)	0.31	2000
S42	Pellet	Solid-state reaction	Ta	1000	4	Cubic	8.70E-04	0.22	
S43	Pellet	Solid-state reaction	Ta, Al	1100	6	Cubic	1.90E-04	0.37	1500
S44	Pellet	Solid-state reaction	Ta, Al	1230	20	Cubic	5.20E-04	0.41	5000
S45	Pellet	Solid-state reaction	Ta, Al	1140	9	Cubic	7.40E-04	0.33	
S46	Pellet	Solid-state reaction	Ta, Al (from crucible)	1120	8	Cubic	1.80E-04	0.42	1760
S47	Pellet	Solid-state reaction	Ta, Al (from crucible)	1175	6	Cubic	7.20E-04	0.42	1000
S48	Pellet	Solid-state reaction	Te, Al (from crucible)	1100	15	Cubic	6.99E-05 (30°C)		
S48	Pellet	Solid-state reaction	Te, Al (from crucible)	1100	15	Cubic	1.02E-04 (30°C)	0.38	
S49	Pellet	Solid-state reaction	W, Al (from crucible)	1100	36	Cubic	7.89E-04 (30°C)	0.45	2650
S50	Pellet	Solid-state reaction	Y	1100	12	Cubic	1.00E-06 (23°C)	0.47	
S51	Sheet	Casting + Pressing	Al	1090	1	Cubic + LZO	2.00E-04	0.35	30
S52	Sheet	Casting + Pressing	Ga	1130	0.3	Cubic + Tetragonal	1.30E-03	0.28	25
S53	Sheet	Solid-state reaction	Ta	1140	16	Cubic	1.02E-03		200
S54	Thin film	Aerosol deposition	Al	25	0	Cubic	1.00E-08 (140°C)	1.3	20
S55	Thin film	Sol-gel	Al	600	0.17	LZO	1.67E-06	0.18	0.3
S56	Thin film	Sol-gel	Al	900		Cubic	2.40E-06	0.52	1
S57	Thin film	Pulsed laser deposition (epitaxial)	Al	700		Cubic	1.00E-05	0.52	0.03
S58	Thin film	Pulsed laser deposition	Al	600	24	Cubic + LZO	8.30E-04 (300°C)	1.39	0.38
S59	Thin film	Magnetron sputtering	Al	700	1	Cubic + Tetragonal	1.90E-05	0.48	0.4
S60	Thin film	Magnetron sputtering	Ga	700	2.5	Cubic	1.60E-05 (30°C)	0.66	0.5
S61	Thin film	Magnetron sputtering	None	25	0	Amorphous	4.00E-07	0.7	0.561
S62	Thin film	Pulsed laser deposition	None	800	0.5	Cubic	7.36E-07	0.32	1
S63	Thin film	Sol-gel	None	400		Amorphous	1.00E-06	0.6	0.76
S64	Thin film	Pulsed laser deposition	None	600		Cubic + Tetragonal	1.61E-06	0.35	0.2
S65	Thin film	Laser-assisted chemical vapor deposition	None	700		Tetragonal	4.20E-06	0.5	0.85
S66	Thin film	Aerosol deposition	Ta	300		Cubic	2.40E-06 (27°C)		15
S67	Thin film	Pulsed laser deposition	Ta, Al	300		Amorphous	2.39E-08	0.613	0.3
S68	Thin film	Pulsed laser deposition	Ta, Al	660	0.25	Cubic	2.90E-05	0.46	0.35
S69	Thin film	Magnetron sputtering	Ta, Al	700		Cubic	1.20E-04	0.47	1.8
S70	Thin film	Magnetron sputtering	Ti	300	2	Amorphous	2.83E-06		0.53
S71	Thin film	Sol-gel	Y	800	0.17	Cubic	3.40E-08 (45°C)		0.05

References

- (S1) Almond, D. P.; West, A. R. Measurement of Mechanical and Electrical Relaxations in β -Alumina. *Solid State Ion.* **1981**, *3-4*, 73–77.
- (S2) Almond, D. P.; West, A. R. Impedance and Modulus Spectroscopy of “Real” Dispersive Conductors. *Solid State Ion.* **1983**, *11*, 57–64.
- (S3) Djenadic, R.; Botros, M.; Benel, C.; Clemens, O.; Indris, S.; Choudhary, A.; Bergfeldt, T.; Hahn, H. Nebulized Spray Pyrolysis of Al-Doped $\text{Li}_7\text{La}_3\text{Zr}_2\text{O}_{12}$ Solid Electrolyte for Battery Applications. *Solid State Ion.* **2014**, *263*, 49–56.
- (S4) Shimonishi, Y.; Toda, A.; Zhang, T.; Hirano, A.; Imanishi, N.; Yamamoto, O.; Takeda, Y. Synthesis of Garnet-Type $\text{Li}_{7-x}\text{La}_3\text{Zr}_2\text{O}_{12-1/2x}$ and Its Stability in Aqueous Solutions. *Solid State Ion.* **2011**, *183*, 48–53.
- (S5) Kotobuki, M.; Kanamura, K.; Sato, Y.; Yoshida, T. Fabrication of All-Solid-State Lithium Battery with Lithium Metal Anode Using Al_2O_3 -Added $\text{Li}_7\text{La}_3\text{Zr}_2\text{O}_{12}$ Solid Electrolyte. *J. Power Sources* **2011**, *196*, 7750–7754.
- (S6) Jin, Y.; McGinn, P. J. Al-Doped $\text{Li}_7\text{La}_3\text{Zr}_2\text{O}_{12}$ Synthesized by a Polymerized Complex Method. *J. Power Sources* **2011**, *196*, 8683–8687.
- (S7) Matsuda, Y.; Sakamoto, K.; Matsui, M.; Yamamoto, O.; Takeda, Y.; Imanishi, N. Phase Formation of a Garnet-Type Lithium-Ion Conductor $\text{Li}_{7-3x}\text{Al}_x\text{La}_3\text{Zr}_2\text{O}_{12}$. *Solid State Ion.* **2015**, *277*, 23–29.
- (S8) Hu, Z.; Liu, H.; Ruan, H.; Hu, R.; Su, Y.; Zhang, L. High Li-Ion Conductivity of Al-Doped $\text{Li}_7\text{La}_3\text{Zr}_2\text{O}_{12}$ Synthesized by Solid-State Reaction. *Ceramics International* **2016**, *42*, 12156–12160.
- (S9) Chen, R.-J.; Huang, M.; Huang, W.-Z.; Shen, Y.; Lin, Y.-H.; Nan, C.-W. Effect of

Calcining and Al Doping on Structure and Conductivity of $\text{Li}_7\text{La}_3\text{Zr}_2\text{O}_{12}$. *Solid State Ion.* **2014**, *265*, 7–12.

- (S10) Kumazaki, S.; Iriyama, Y.; Kim, K.-H.; Murugan, R.; Tanabe, K.; Yamamoto, K.; Hirayama, T.; Ogumi, Z. High Lithium Ion Conductive $\text{Li}_7\text{La}_3\text{Zr}_2\text{O}_{12}$ by Inclusion of Both Al and Si. *Electrochem. Commun.* **2011**, *13*, 509–512.
- (S11) Suzuki, Y.; Kami, K.; Watanabe, K.; Watanabe, A.; Saito, N.; Ohnishi, T.; Takada, K.; Sudo, R.; Imanishi, N. Transparent Cubic Garnet-Type Solid Electrolyte of Al_2O_3 -Doped $\text{Li}_7\text{La}_3\text{Zr}_2\text{O}_{12}$. *Solid State Ion.* **2015**, *278*, 172–176.
- (S12) Sudo, R.; Nakata, Y.; Ishiguro, K.; Matsui, M.; Hirano, A.; Takeda, Y.; Yamamoto, O.; Imanishi, N. Interface Behavior between Garnet-Type Lithium-Conducting Solid Electrolyte and Lithium Metal. *Solid State Ion.* **2014**, *262*, 151–154.
- (S13) Rettenwander, D.; Redhammer, G.; Preishuber-Pflügl, F.; Cheng, L.; Miara, L.; Wagner, R.; Welzl, A.; Suard, E.; Doeuff, M. M.; Wilkening, M.; Fleig, J.; Amthauer, G. Structural and Electrochemical Consequences of Al and Ga Cosubstitution in $\text{Li}_7\text{La}_3\text{Zr}_2\text{O}_{12}$ Solid Electrolytes. *Chem. Mater.* **2016**, *28*, 2384–2392.
- (S14) Botros, M.; Djenadic, R.; Clemens, O.; Möller, M.; Hahn, H. Field Assisted Sintering of Fine-Grained $\text{Li}_{7-3x}\text{La}_3\text{Zr}_2\text{Al}_x\text{O}_{12}$ Solid Electrolyte and the Influence of the Microstructure on the Electrochemical Performance. *J. Power Sources* **2016**, *309*, 108–115.
- (S15) Kim, Y.; Jo, H.; Allen, J. L.; Choe, H.; Wolfenstine, J.; Sakamoto, J. The Effect of Relative Density on the Mechanical Properties of Hot-Pressed Cubic $\text{Li}_7\text{La}_3\text{Zr}_2\text{O}_{12}$. *J. Am. Ceram. Soc.* **2016**, *99*, 1367–1374.
- (S16) Tsai, C.-L.; Dashjav, E.; Hammer, E.-M.; Finsterbusch, M.; Tietz, F.; Uhlenbruck, S.; Buchkremer, H. P. High Conductivity of Mixed Phase Al-Substituted $\text{Li}_7\text{La}_3\text{Zr}_2\text{O}_{12}$. *J. Electroceramics* **2015**, *35*, 25–32.

- (S17) Pesci, F. M.; Brugge, R. H.; Hekselman, A. K. O.; Cavallaro, A.; Chater, R. J.; Aguadero, A. Elucidating the Role of Dopants in the Critical Current Density for Dendrite Formation in Garnet Electrolytes. *J. Mater. Chem. A* **2018**, *6*, 19817–19827.
- (S18) Buschmann, H.; Dölle, J.; Berendts, S.; Kuhn, A.; Bottke, P.; Wilkening, M.; Heijmans, P.; Senyshyn, A.; Ehrenberg, H.; Lotnyk, A.; Duppel, V.; Kienle, L.; Janek, J. Structure and Dynamics of the Fast Lithium Ion Conductor “ $\text{Li}_7\text{La}_3\text{Zr}_2\text{O}_{12}$ ”. *Phys. Chem. Chem. Phys.* **2011**, *13*, 19378.
- (S19) Rangasamy, E.; Wolfenstine, J.; Sakamoto, J. The Role of Al and Li Concentration on the Formation of Cubic Garnet Solid Electrolyte of Nominal Composition $\text{Li}_7\text{La}_3\text{Zr}_2\text{O}_{12}$. *Solid State Ion.* **2012**, *206*, 28–32.
- (S20) van den Broek, J.; Afyon, S.; Rupp, J. L. M. Interface-Engineered All-Solid-State Li-Ion Batteries Based on Garnet-Type Fast Li^+ Conductors. *Adv. Energy Mater.* **2016**, *6*, 1600736.
- (S21) Zhang, Y.; Chen, F.; Tu, R.; Shen, Q.; Zhang, X.; Zhang, L. Effect of Lithium Ion Concentration on the Microstructure Evolution and Its Association with the Ionic Conductivity of Cubic Garnet-Type Nominal $\text{Li}_7\text{Al}_{0.25}\text{La}_3\text{Zr}_2\text{O}_{12}$ Solid Electrolytes. *Solid State Ion.* **2016**, *284*, 53–60.
- (S22) Zhang, Y.; Chen, F.; Tu, R.; Shen, Q.; Zhang, L. Field Assisted Sintering of Dense Al-Substituted Cubic Phase $\text{Li}_7\text{La}_3\text{Zr}_2\text{O}_{12}$ Solid Electrolytes. *J. Power Sources* **2014**, *268*, 960–964.
- (S23) Li, Y.; Han, J.-T.; Wang, C.-A.; Vogel, S. C.; Xie, H.; Xu, M.; Goodenough, J. B. Ionic Distribution and Conductivity in Lithium Garnet $\text{Li}_7\text{La}_3\text{Zr}_2\text{O}_{12}$. *J. Power Sources* **2012**, *209*, 278–281.
- (S24) Huang, M.; Liu, T.; Deng, Y.; Geng, H.; Shen, Y.; Lin, Y.; Nan, C.-W. Effect

of Sintering Temperature on Structure and Ionic Conductivity of $\text{Li}_{7-x}\text{La}_3\text{Zr}_2\text{O}_{12-0.5x}$ ($X=0.5 \sim 0.7$) Ceramics. *Solid State Ion.* **2011**, *204-205*, 41–45.

- (S25) Murugan, R.; Thangadurai, V.; Weppner, W. Fast Lithium Ion Conduction in Garnet-Type $\text{Li}_7\text{La}_3\text{Zr}_2\text{O}_{12}$. *Angew. Chem. Int. Ed.* **2007**, *46*, 7778–7781.
- (S26) Xia, W.; Xu, B.; Duan, H.; Guo, Y.; Kang, H.; Li, H.; Liu, H. Ionic Conductivity and Air Stability of Al-Doped $\text{Li}_7\text{La}_3\text{Zr}_2\text{O}_{12}$ Sintered in Alumina and Pt Crucibles. *ACS Appl. Mater. Interfaces* **2016**, *8*, 5335–5342.
- (S27) Rangasamy, E.; Wolfenstine, J.; Allen, J.; Sakamoto, J. The Effect of 24c-Site (A) Cation Substitution on the Tetragonal–Cubic Phase Transition in $\text{Li}_{7-x}\text{La}_{3-x}\text{A}_x\text{Zr}_2\text{O}_{12}$ Garnet-Based Ceramic Electrolyte. *J. Power Sources* **2013**, *230*, 261–266.
- (S28) Wolfenstine, J.; Ratchford, J.; Rangasamy, E.; Sakamoto, J.; Allen, J. L. Synthesis and High Li-Ion Conductivity of Ga-Stabilized Cubic $\text{Li}_7\text{La}_3\text{Zr}_2\text{O}_{12}$. *Mater. Chem. Phys.* **2012**, *134*, 571–575.
- (S29) El Shinawi, H.; Janek, J. Stabilization of Cubic Lithium-Stuffed Garnets of the Type “ $\text{Li}_7\text{La}_3\text{Zr}_2\text{O}_{12}$ ” by Addition of Gallium. *J. Power Sources* **2013**, *225*, 13–19.
- (S30) Matsuda, Y.; Sakaida, A.; Sugimoto, K.; Mori, D.; Takeda, Y.; Yamamoto, O.; Imanishi, N. Sintering Behavior and Electrochemical Properties of Garnet-like Lithium Conductor $\text{Li}_{6.25}\text{Li}_{0.25}\text{La}_3\text{Zr}_2\text{O}_{12}$ (M: Al^{3+} and Ga^{3+}). *Solid State Ion.* **2017**, *311*, 69–74.
- (S31) Howard, M. A.; Clemens, O.; Kendrick, E.; Knight, K. S.; Apperley, D. C.; Anderson, P. A.; Slater, P. R. Effect of Ga Incorporation on the Structure and Li Ion Conductivity of $\text{Li}_7\text{La}_3\text{Zr}_2\text{O}_{12}$. *Dalton Trans.* **2012**, *41*, 12048–12053.
- (S32) Bernuy-Lopez, C.; Manalastas, W.; Lopez del Amo, J. M.; Aguadero, A.; Aguesse, F.;

- Kilner, J. A. Atmosphere Controlled Processing of Ga-Substituted Garnets for High Li-Ion Conductivity Ceramics. *Chem. Mater.* **2014**, *26*, 3610–3617.
- (S33) Toda, S.; Ishiguro, K.; Shimonishi, Y.; Hirano, A.; Takeda, Y.; Yamamoto, O.; Imanishi, N. Low Temperature Cubic Garnet-Type CO₂-Doped Li₇La₃Zr₂O₁₂. *Solid State Ion.* **2013**, *233*, 102–106.
- (S34) Xie, H.; Li, Y.; Goodenough, J. B. Low-Temperature Synthesis of Li₇La₃Zr₂O₁₂ with Cubic Garnet-Type Structure. *Mater. Res. Bull.* **2012**, *47*, 1229–1232.
- (S35) Ohta, S.; Kobayashi, T.; Asaoka, T. High Lithium Ionic Conductivity in the Garnet-Type Oxide Li_{7-X}La₃(Zr_{2-X},Nb_X)O₁₂ (X=0-2). *J. Power Sources* **2011**, *196*, 3342–3345.
- (S36) Kokal, I.; Somer, M.; Notten, P. H. L.; Hintzen, H. T. Sol–Gel Synthesis and Lithium Ion Conductivity of Li₇La₃Zr₂O₁₂ with Garnet-Related Type Structure. *Solid State Ion.* **2011**, *185*, 42–46.
- (S37) Awaka, J.; Kijima, N.; Hayakawa, H.; Akimoto, J. Synthesis and Structure Analysis of Tetragonal Li₇La₃Zr₂O₁₂ with the Garnet-Related Type Structure. *J. Solid State Chem.* **2009**, *182*, 2046–2052.
- (S38) Il'ina, E. A.; Andreev, O. L.; Antonov, B. D.; Batalov, N. N. Morphology and Transport Properties of the Solid Electrolyte Li₇La₃Zr₂O₁₂ Prepared by the Solid-State and Citrate–Nitrate Methods. *J. Power Sources* **2012**, *201*, 169–173.
- (S39) Wolfenstine, J.; Rangasamy, E.; Allen, J. L.; Sakamoto, J. High Conductivity of Dense Tetragonal Li₇La₃Zr₂O₁₂. *J. Power Sources* **2012**, *208*, 193–196.
- (S40) Ramakumar, S.; Satyanarayana, L.; Manorama, S. V.; Murugan, R. Structure and Li⁺ Dynamics of Sb-Doped Li₇La₃Zr₂O₁₂ Fast Lithium Ion Conductors. *Phys. Chem. Chem. Phys.* **2013**, *15*, 11327–11338.

- (S41) Dumon, A.; Huang, M.; Shen, Y.; Nan, C.-W. High Li Ion Conductivity in Strontium Doped $\text{Li}_7\text{La}_3\text{Zr}_2\text{O}_{12}$ Garnet. *Solid State Ion.* **2013**, *243*, 36–41.
- (S42) Allen, J.; Wolfenstine, J.; Rangasamy, E.; Sakamoto, J. Effect of Substitution (Ta, Al, Ga) on the Conductivity of $\text{Li}_7\text{La}_3\text{Zr}_2\text{O}_{12}$. *J. Power Sources* **2012**, *206*, 315–319.
- (S43) Cheng, L.; Park, J. S.; Hou, H.; Zorba, V.; Chen, G.; Richardson, T.; Cabana, J.; Russo, R.; Doeff, M. Effect of Microstructure and Surface Impurity Segregation on the Electrical and Electrochemical Properties of Dense Al-Substituted $\text{Li}_7\text{La}_3\text{Zr}_2\text{O}_{12}$. *J. Mater. Chem. A* **2014**, *2*, 172–181.
- (S44) Buschmann, H.; Berendts, S.; Mogwitz, B.; Janek, J. Lithium Metal Electrode Kinetics and Ionic Conductivity of the Solid Lithium Ion Conductors “ $\text{Li}_7\text{La}_3\text{Zr}_2\text{O}_{12}$ ” and $\text{Li}_{7-x}\text{La}_3\text{Zr}_{2-x}\text{Ta}_x\text{O}_{12}$ with Garnet-Type Structure. *J. Power Sources* **2012**, *206*, 236–244.
- (S45) Li, Y.; Wang, Z.; Li, C.; Cao, Y.; Guo, X. Densification and Ionic-Conduction Improvement of Lithium Garnet Solid Electrolytes by Flowing Oxygen Sintering. *J. Power Sources* **2014**, *248*, 642–646.
- (S46) Li, Y.; Wang, C.-A.; Xie, H.; Cheng, J.; Goodenough, J. B. High Lithium Ion Conduction in Garnet-Type $\text{Li}_6\text{La}_3\text{ZrTaO}_{12}$. *Electrochem. Commun.* **2011**, *13*, 1289–1292.
- (S47) Cao, Y.; Li, Y.-Q.; Guo, X.-X. Densification and Lithium Ion Conductivity of Garnet-Type $\text{Li}_{7-x}\text{La}_3\text{Zr}_{2-x}\text{Ta}_x\text{O}_{12}$ ($x = 0.25$) Solid Electrolytes. *Chin. Phys. B* **2013**, *22*, 078201.
- (S48) Deviannapoorani, C.; Dhivya, L.; Ramakumar, S.; Murugan, R. Lithium Ion Transport Properties of High Conductive Tellurium Substituted $\text{Li}_7\text{La}_3\text{Zr}_2\text{O}_{12}$ Cubic Lithium Garnets. *J. Power Sources* **2013**, *240*, 18–25.

- (S49) Dhivya, L.; Janani, N.; Palanivel, B.; Murugan, R. Li⁺ Transport Properties of W Substituted Li₇La₃Zr₂O₁₂ Cubic Lithium Garnets. *AIP Adv.* **2013**, *3*, 082115.
- (S50) Hitz, G. T.; Wachsman, E. D.; Thangadurai, V. Highly Li-Stuffed Garnet-Type Li_{7+x}La₃Zr_{2-x}Y_xO₁₂. *J. Electrochem. Soc.* **2013**, *160*, A1248–A1255.
- (S51) Yi, E.; Wang, W.; Kieffer, J.; Laine, R. M. Flame Made Nanoparticles Permit Processing of Dense, Flexible, Li⁺ Conducting Ceramic Electrolyte Thin Films of Cubic-Li₇La₃Zr₂O₁₂ (c-LLZO). *J. Mater. Chem. A* **2016**, *4*, 12947–12954.
- (S52) Yi, E.; Wang, W.; Kieffer, J.; Laine, R. M. Key Parameters Governing the Densification of Cubic-Li₇La₃Zr₂O₁₂ Li⁺ Conductors. *J. Power Sources* **2017**, *352*, 156–164.
- (S53) Liu, K.; Wang, C.-A. Garnet-Type Li_{6.4}La₃Zr_{1.4}Ta_{0.6}O₁₂ Thin Sheet: Fabrication and Application in Lithium–Hydrogen Peroxide Semi-Fuel Cell. *Electrochem. Commun.* **2014**, *48*, 147–150.
- (S54) Ahn, C.-W.; Choi, J.-J.; Ryu, J.; Hahn, B.-D.; Kim, J.-W.; Yoon, W.-H.; Choi, J.-H.; Park, D.-S. Microstructure and Ionic Conductivity in Li₇La₃Zr₂O₁₂ Film Prepared by Aerosol Deposition Method. *J. Electrochem. Soc.* **2015**, *162*, A60–A63.
- (S55) Chen, R.-J.; Huang, M.; Huang, W.-Z.; Shen, Y.; Lin, Y.-H.; Nan, C.-W. Sol–Gel Derived Li–La–Zr–O Thin Films as Solid Electrolytes for Lithium-Ion Batteries. *J. Mater. Chem. A* **2014**, *2*, 13277.
- (S56) Tadanaga, K.; Egawa, H.; Hayashi, A.; Tatsumisago, M.; Mosa, J.; Aparicio, M.; Duran, A. Preparation of Lithium Ion Conductive Al-Doped Li₇La₃Zr₂O₁₂ Thin Films by a Sol–Gel Process. *J. Power Sources* **2015**, *273*, 844–847.
- (S57) Kim, S.; Hirayama, M.; Taminato, S.; Kanno, R. Epitaxial Growth and Lithium Ion Conductivity of Lithium-Oxide Garnet for an All Solid-State Battery Electrolyte. *Dalton Trans.* **2013**, *42*, 13112.

- (S58) Rawlence, M.; Garbayo, I.; Buecheler, S.; Rupp, J. L. M. On the Chemical Stability of Post-Lithiated Garnet Al-Stabilized $\text{Li}_7\text{La}_3\text{Zr}_2\text{O}_{12}$ Solid State Electrolyte Thin Films. *Nanoscale* **2016**, *8*, 14746–14753.
- (S59) Sastre, J.; Lin, T.-Y.; Filippin, A. N.; Priebe, A.; Avancini, E.; Michler, J.; Tiwari, A. N.; Romanyuk, Y. E.; Buecheler, S. Aluminum-Assisted Densification of Cospattered Lithium Garnet Electrolyte Films for Solid-State Batteries. *ACS Appl. Energy Mater.* **2019**, *2*, 8511–8524.
- (S60) Rawlence, M.; Filippin, A. N.; Wäckerlin, A.; Lin, T.-Y.; Cuervo-Reyes, E.; Remhof, A.; Battaglia, C.; Rupp, J. L. M.; Buecheler, S. Effect of Gallium Substitution on Lithium-Ion Conductivity and Phase Evolution in Sputtered $\text{Li}_{7-3x}\text{Ga}_x\text{La}_3\text{Zr}_2\text{O}_{12}$ Thin Films. *ACS Appl. Mater. Interfaces* **2018**, *10*, 13720–13728.
- (S61) Kalita, D.; Lee, S.; Lee, K.; Ko, D.; Yoon, Y. Ionic Conductivity Properties of Amorphous Li-La-Zr-O Solid Electrolyte for Thin Film Batteries. *Solid State Ion.* **2012**, *229*, 14–19.
- (S62) Tan, J.; Tiwari, A. Fabrication and Characterization of $\text{Li}_7\text{La}_3\text{Zr}_2\text{O}_{12}$ Thin Films for Lithium Ion Battery. *ECS Solid State Lett.* **2012**, *1*, Q57–Q60.
- (S63) Zarabian, M.; Bartolini, M.; Pereira-Almao, P.; Thangadurai, V. X-Ray Photoelectron Spectroscopy and AC Impedance Spectroscopy Studies of Li-La-Zr-O Solid Electrolyte Thin Film/ LiCoO_2 Cathode Interface for All-Solid-State Li Batteries. *J. Electrochem. Soc.* **2017**, *164*, A1133–A1139.
- (S64) Park, J. S.; Cheng, L.; Zorba, V.; Mehta, A.; Cabana, J.; Chen, G.; Doeff, M. M.; Richardson, T. J.; Park, J. H.; Son, J.-W.; Hong, W.-S. Effects of Crystallinity and Impurities on the Electrical Conductivity of Li-La-Zr-O Thin Films. *Thin Solid Films* **2015**, *576*, 55–60.

- (S65) Loho, C.; Djenadic, R.; Bruns, M.; Clemens, O.; Hahn, H. Garnet-Type $\text{Li}_7\text{La}_3\text{Zr}_2\text{O}_{12}$ Solid Electrolyte Thin Films Grown by CO₂-Laser Assisted CVD for All-Solid-State Batteries. *J. Electrochem. Soc.* **2017**, *164*, A6131–A6139.
- (S66) Inada, R.; Okada, T.; Bando, A.; Tojo, T.; Sakurai, Y. Properties of Garnet-Type $\text{Li}_6\text{La}_3\text{ZrTaO}_{12}$ Solid Electrolyte Films Fabricated by Aerosol Deposition Method. *Prog. Nat. Sci. Mater. Int.* **2017**, *27*, 350–355.
- (S67) Garbayo, I.; Struzik, M.; Bowman, W. J.; Pfenninger, R.; Stilp, E.; Rupp, J. L. M. Glass-Type Polyamorphism in Li-Garnet Thin Film Solid State Battery Conductors. *Adv. Energy Mater.* **2018**, *1702265*.
- (S68) Pfenninger, R.; Struzik, M.; Garbayo, I.; Stilp, E.; Rupp, J. L. M. A Low Ride on Processing Temperature for Fast Lithium Conduction in Garnet Solid-State Battery Films. *Nat. Energy* **2019**, *4*, 475–483.
- (S69) Lobe, S.; Dellen, C.; Finsterbusch, M.; Gehrke, H. G.; Sebold, D.; Tsai, C. L.; Uhlenbruck, S.; Guillon, O. Radio Frequency Magnetron Sputtering of $\text{Li}_7\text{La}_3\text{Zr}_2\text{O}_{12}$ Thin Films for Solid-State Batteries. *J. Power Sources* **2016**, *307*, 684–689.
- (S70) Nong, J.; Xu, H.; Yu, Z.; Zhu, G.; Yu, A. Properties and Preparation of Li-La-Ti-Zr-O Thin Film Electrolyte. *Mater. Lett.* **2015**, *154*, 167–169.
- (S71) Bitzer, M.; Van Gestel, T.; Uhlenbruck, S.; Hans-Peter-Buchkremer, Sol-Gel Synthesis of Thin Solid $\text{Li}_7\text{La}_3\text{Zr}_2\text{O}_{12}$ Electrolyte Films for Li-Ion Batteries. *Thin Solid Films* **2016**, *615*, 128–134.